



Power Electronic Systems  
Laboratory

© 2016 IEEE

IEEE Journal of Emerging and Selected Topics on Power Electronics (JESTPE), Vol. 4, No. 4, pp. 1406-1415, December 2016

## Comprehensive Evaluation of Rectangular and Double-D Coil Geometry for 50 kW/85 kHz IPT System

R. Bosshard,  
U. Iruretagoyena  
J. W. Kolar

This material is published in order to provide access to research results of the Power Electronic Systems Laboratory / D-ITET / ETH Zurich. Internal or personal use of this material is permitted. However, permission to reprint/republish this material for advertising or promotional purposes or for creating new collective works for resale or redistribution must be obtained from the copyright holder. By choosing to view this document, you agree to all provisions of the copyright laws protecting it.



Eidgenössische Technische Hochschule Zürich  
Swiss Federal Institute of Technology Zurich

# Comprehensive Evaluation of Rectangular and Double-D Coil Geometry for 50 kW/85 kHz IPT System

Roman Bosshard, *Student Member, IEEE*, Ugaitz Iruretagoyena, and Johann W. Kolar, *Fellow, IEEE*

**Abstract**—In this paper, the influence of the inductive power transfer (IPT) coil geometry on the performance factors efficiency, power density, and stray field is studied for a public transport electric vehicle battery charging system. IPT coil geometries with rectangular winding and with double-D winding are compared based on the Pareto fronts obtained from a multi-objective optimization. In order to study the effect of the winding layout experimentally, two full-scale 50 kW/85 kHz hardware prototypes with the same outer coil dimensions ( $410 \times 760 \times 60 \text{ mm}^3$ ) and ferrite core structure are constructed. For both the prototypes, the measured dc–dc efficiency is approximately 95.5% at 50 kW with a 160 mm air gap and ideally positioned coils, which confirms the calculations. The positioning tolerance of the double-D prototype is inferior, because with coil misalignment the efficiency decays faster than for the rectangular winding prototype. Flux density measurements show that both the prototypes fulfill the ICNIRP 2010 standard at 800 mm lateral distance from the coil center. However, the measured magnetic stray field is a factor of two lower for the double-D winding, which is a key advantage in high-power applications.

**Index Terms**—Pareto optimization, electric vehicles, inductive power transmission.

## I. INTRODUCTION

CONTACTLESS charging of electric vehicle (EV) batteries by inductive power transfer (IPT) offers unique advantages compared with conventional conductive chargers. Due to the absence of a galvanic connection, the charging process requires no user interaction and no moving mechanical components. For public transport systems, e.g., public buses or tramways, this makes possible a fully automated *opportunity charging* at bus stations, taxicab stands, or traffic lights [1]–[4]. The frequent recharging enables a reduction in the volume and weight of the on-board energy storage, as well as an increase in the battery lifetime, because of the lower depth of discharge.

Manuscript received May 2, 2016; revised June 20, 2016 and August 6, 2016; accepted August 9, 2016. Date of publication August 12, 2016; date of current version October 28, 2016. This work was supported by the ABB Switzerland Ltd. Recommended for publication by Associate Editor Chun T. Rim.

R. Bosshard was with the Power Electronic Systems Laboratory, ETH Zürich, 8092 Zürich, Switzerland. He is now with ABB Switzerland Ltd., ABB Switzerland Ltd., 5300 Turgi, Switzerland (e-mail: roman.bosshard@gmail.com).

U. Iruretagoyena is with the IK4-Ikerlan Technology Research Center, 20500 Mondragón, Spain (e-mail: uiruretagoyena@ikerlan.es).

J. W. Kolar is with the Power Electronic Systems Laboratory, ETH Zürich, 8092 Zürich, Switzerland (e-mail: kolar@lem.ee.ethz.ch).

Color versions of one or more of the figures in this paper are available online at <http://ieeexplore.ieee.org>.

Digital Object Identifier 10.1109/JESTPE.2016.2600162

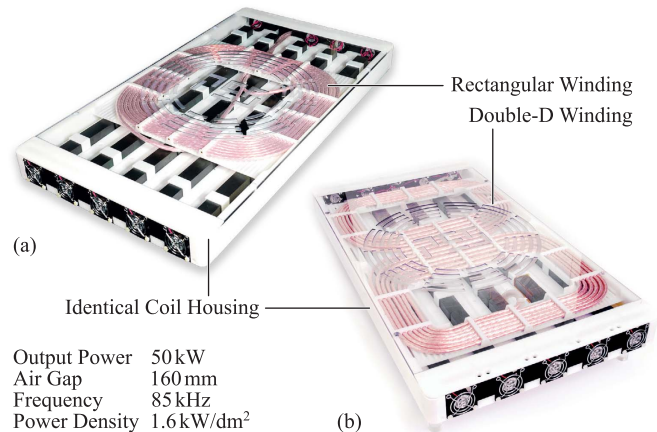


Fig. 1. Photographs of the two investigated 50 kW/85 kHz hardware prototypes. (a) Rectangular winding layout employed in [17]. (b) Double-D winding layout with identical ferrite core structure, coil housing, and area-related power density. Transmitter and receiver coils of the same type in both the cases.

One of the main performance requirements for IPT systems in automotive applications is a high efficiency, for minimizing the energy costs of the charging process and for simplifying the thermal management. In addition, a high power density of the on-board components is needed, due to the limited available construction volume on the EV. Furthermore, the high-frequency electromagnetic stray fields have to fulfill the relevant safety standards [5] and a high positioning tolerance is needed in practice.

A number of design options for the IPT coil geometry of contactless EV chargers have been proposed [6]–[12]. In particular, the *double-D* winding layout of [12] is extensively discussed in the recent literature. Although the different IPT coil geometries are compared in a number of papers [13]–[16], their individual benefits with respect to the main performance factors of efficiency, power density, and stray field are not fully clear. In some publications, only specific realization examples are analyzed, instead of comparing the best possible performance that could be reached with fully optimized designs. It is shown in [17], for the 50 kW/85 kHz IPT demonstrator in Fig. 1(a), that the performance factors of efficiency, power density, and stray field are interlinked by design tradeoffs. Therefore, for a fair comparison of IPT coil geometries, a multi-objective analysis as proposed in [17]–[19] is necessary. The method allows calculating the physical

performance limit, termed as the Pareto front, for each IPT coil geometry. Only a comparison of the Pareto fronts of the geometries can give a comprehensive picture of the advantages and disadvantages of the different design options.

The main aim of this paper is to provide a comprehensive comparison between the rectangular winding in Fig. 1(a) and the widely discussed double-D winding for a high-power, public transport EV application. Therefore, in this paper the approach of [17] is applied for the optimization of a second hardware prototype. A double-D coil is designed for 50 kW output power at a 160 mm air gap, a transmission frequency of 85 kHz as proposed in [20], and with an identical ferrite core structure and coil housing as the existing prototype. During the optimization process, the Pareto fronts of the two IPT coil geometries are calculated and the key differences are discussed in detail. Since both the prototypes are designed for the same output power and cover the same footprint area on the vehicle, the area-related power density is identical for both the prototypes. This ensures the best comparability of the experimental results. At the end of this paper, an extensive experimental evaluation of the two prototypes is presented.

The analysis is organized into four sections. Section II starts with a classification of the different IPT coil geometries that exist in the literature into the two major categories E-type and C-type IPT coils, according to the shape of their reluctance path. The advantages and disadvantages of each category are discussed on a conceptual level. During the discussion, it becomes clear that only a multi-objective analysis can provide a comprehensive evaluation as neither category is clearly superior. In Section III, the multi-objective optimization of the IPT coils with a rectangular winding (E-type) and with a double-D winding (C-type) is presented. The two geometries are compared with respect to the attainable efficiency, power density, and magnetic stray field, using the Pareto front as proposed in [17]. In Section IV, a comprehensive experimental investigation is conducted using the IPT test setup described in [21]. Measurements of the magnetic coupling factor, as well as measurements of the dc-dc efficiency and of the magnetic stray field up to 50 kW are presented. Finally, in Section V, the key differences between the IPT coils with rectangular winding and with double-D winding are summarized, and the general conclusions for high-power EV applications are drawn.

## II. CLASSIFICATION OF IPT COIL GEOMETRIES

A large number of design options have been proposed for the IPT coil geometry of contactless EV chargers. However, an intuitive classification of the different geometries into types with similar physical properties is yet missing. Therefore, in this section, the coil geometries found in the recent literature are classified into E-type and C-type IPT coils, according to the shape of their reluctance path. The key differences between the two types are discussed on a conceptual level. Later in this paper, they are investigated in detail using the Pareto analysis.

### A. Classification Based on Reluctance Path

IPT coils for contactless EV chargers typically employ ferrite core material for guiding the high-frequency magnetic

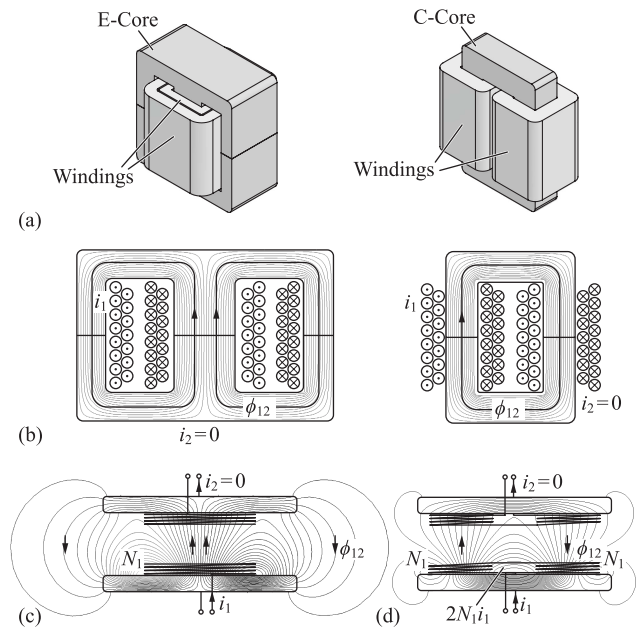


Fig. 2. (a) Schematic of conventional power transformers with E- or C-cores. (b) 2-D cross-sectional view with FEM-calculated field lines. (c) E-type and (d) C-type IPT coil designs with FEM-calculated field lines.

fields and for increasing the magnetic coupling. The core shapes for IPT coils resemble those of conventional, single-phase transformers. Power transformers can be divided into two main categories, depending on whether the 2-D projection of their reluctance path shows two loops as for E-cores, or only a single loop as for C-cores (see Fig. 2(a) and (b)). Given the similarity of the cross-sectional view, also pot cores can be understood as E-cores and toroidal cores are essentially C-cores with a circular shape.

Similarly, IPT coil geometries can be classified according to their magnetic field distribution. In a 2-D view, the commonly employed spiral coil on a ferrite core [10], [17], [18], [22], [23] as well as the geometry in [24] have a field distribution similar to that in Fig. 2(c). These geometries are termed as E-type IPT coils, in reference to the E-core transformer.

The double-D coil geometry discussed in [12] and the structure in [25] show a 2-D field distribution similar to Fig. 2(d). Analogous to the C-core transformer, this IPT coil geometry is termed as a C-type IPT coil. The IPT coil geometries shown in [6], [9], and [26], which consist of a winding placed around a planar core similar to a solenoid inductor, also have a reluctance path with only a single loop and therefore belong to the category of C-type IPT coils. However, the placement of the winding around the core leads to a significant increase in the magnetic stray field, particularly at the backsides of the IPT coils [12]. Therefore, this geometry is not discussed in this paper.

### B. Differences Between E-Type and C-Type IPT Coils

The reluctance of a magnetic path is proportional to the path length and is inversely proportional to the magnetic cross section. Because of the increasing magnetic cross section, the

field lines that extend to the left and right sides of the cores in the E-type geometry of Fig. 2(c) encounter a similar reluctance as those following a more direct path. Hence, for an E-type core geometry, the environment immediately surrounding the coils is utilized by the flux and is part of the magnetic circuit.

In the C-type geometry in Fig. 2(d), the winding senses of the two transmitter coils are such that the flux exhibits the opposite orientation at each side. In practice, the windings are typically connected in series. The magnetic core guides the flux from the coil on one side to the coil on the other side. The reluctance of any magnetic path spreading out at the backside or at the sides of the coils is larger than for the direct path. Hence, the reluctance path is fully contained within the IPT coil structure and the environment surrounding the IPT coils is not a part of the magnetic circuit. It is therefore expected that the magnetic stray field of a C-type IPT coil is smaller than for an E-type IPT coil.

The maximum efficiency of an IPT system with optimally designed inductance values and a series or parallel resonant compensation of the receiver is given by the product of the magnetic coupling  $k$  and the quality factor  $Q$  of the IPT coils as [18], [27]–[29]

$$\eta_{\max} = \frac{(kQ)^2}{(1 + \sqrt{1 + (kQ)^2})^2} \approx 1 - \frac{2}{kQ}. \quad (1)$$

For an exact calculation of the figure-of-merit  $FOM = kQ$ , 3-D finite-element method (FEM) calculations are used later in this paper. Already, a simplified analysis based on 2-D FEM simulations reveals that the magnetic coupling is similar for both the coil geometries without coil misalignment. However, the magnetic coupling is highly sensitive to the positioning of the IPT coils. Given that the two coils of the C-type geometry require smaller outer diameters for fitting on the same core than the winding of the E-type geometry, the misalignment tolerance is expected to be lower.

The quality factor  $Q$  describes the power losses in the litz wire windings, the ferrite cores, and the shielding, which is commonly employed at the backside of IPT coils in order to prevent eddy currents in the EV chassis and to reduce the stray field in the passenger cabin (see Fig. 6(a)). In the windings, high-frequency losses are caused by the skin effect and by external magnetic fields. However, if a finely stranded litz wire is used, these ac effects are minimized and the winding losses are dominated by resistive conduction losses, which like in the dc case depend only on the current, the material conductivity, the copper cross section, and the conductor length. If the same number of turns and the same transmitter current is assumed for both the IPT coil geometries, which results in an approximately equal stored magnetic energy for the prototypes investigated in this paper, the copper losses are higher for a C-type coil geometry due to the (approximately 10%–20%) increased conductor length needed for forming two coils instead of just one coil. For the core losses, the magnetic flux density in the core must be compared. Under the same assumptions, a C-type geometry experiences a higher magnetic flux density in the central region of the core, because the Ampère-turns are twice that of the outer region as a result of the two coils that form the C-type winding. Since according

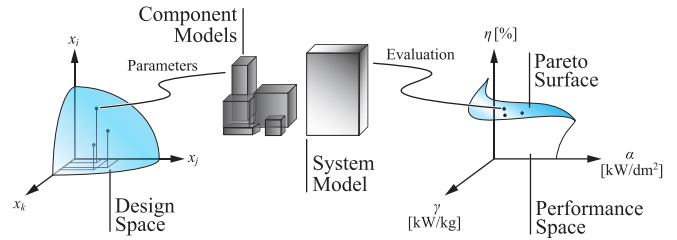


Fig. 3. Multi-objective optimization: component and system models map the parameters of the design space into a multidimensional performance space, where a Pareto surface describes the maximum performance of the system.

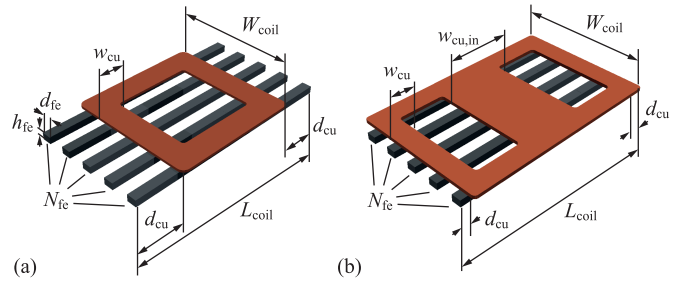


Fig. 4. Degrees-of-freedom considered for the optimization of the IPT coil geometry with (a) rectangular winding and (b) double-D winding.

to the Steinmetz equation the core losses are proportional to the flux density to the power of approximately 2.3 for typical power ferrites, they are expected to be higher for C-type IPT coils.

Clearly, these considerations are only conceptual and depend on the specific parameters of each coil design. More detailed results are obtained when comparing the physical performance boundaries, or Pareto fronts, of E-type and C-type IPT coil geometries. Hence, in the following sections, a representative of each category is selected and analyzed using the multi-objective design approach in [17]–[19]. The results for the prototype in [17] are shown as the example of an E-type IPT coil. For the C-type IPT coil, a second prototype with a double-D winding is optimized for comparison.

### III. MULTI-OBJECTIVE COIL OPTIMIZATION

In this section, the IPT coil geometry with rectangular winding (E-type) in [17] is compared with a coil geometry with double-D winding (C-type) in a multi-objective analysis. The Pareto fronts are derived for both the cases and are used to discuss the advantages and disadvantages of each IPT coil geometry.

#### A. Optimization Methodology

The methodology of a multi-objective optimization is illustrated in Fig. 3. A list of parameter values for the available degrees-of-freedom, i.e., the geometry parameters shown in Fig. 4, define the design space for the system. Mathematical models of the power components and of the system as a whole are used to calculate the performance that is obtained for any parameter set contained in the design space. Finally, the calculated performance is analyzed in the

multidimensional performance space, where a Pareto surface describes the maximum attainable performance of the analyzed system.

The key elements of the optimization process are the component and system models. Considering only the resonant circuit of the IPT system, methods are needed for calculating the power losses in the IPT coils and the resonant capacitors. In [17], an approximative analytical model is proposed for calculating the losses in the litz wire windings. The model is based on analytical solutions for the magnetic field obtained on 2-D cut surfaces of the coil geometry. The ac resistance per unit length is calculated on each cut surface using the analytically calculated magnetic field and the models for litz wire losses given in [30]. The total ac resistance is obtained by adding up the partial resistances according to the length contribution of the respective cut surface to the coil geometry. The same approach is applied for the double-D winding, after a suitable modification of the geometry.

The equivalent circuit parameters, the core losses, the eddy current losses in the shielding, and the magnetic stray field are estimated using 3-D FEM simulations in the frequency domain. For the resonant capacitors, the dissipation factor of the data sheet is used [31].

### B. Degrees-of-Freedom and Design Space

The considered degrees-of-freedom are shown in Fig. 4 and the design space is given in Table I. Apart from the outer coil dimensions  $W_{\text{coil}}$  and  $L_{\text{coil}}$ , also the number of ferrite core rods  $N_{\text{fe}}$ , the spreading of the copper conductors  $w_{\text{cu}}$ , and the position of the winding on the core  $d_{\text{cu}}$  are considered. As discussed in [12], the spreading  $w_{\text{cu,in}}$  of the central conductors in the double-D winding is an additional degree-of-freedom with an impact on the magnetic coupling. If the spreading  $w_{\text{cu,in}}$  is small, the reluctance between the two coils of the transmitter or receiver winding becomes smaller as a result of the decreasing length of the magnetic path. For too small values of  $w_{\text{cu,in}}$ , this results in a magnetic short-circuit of the transmitter and a low magnetic coupling. Therefore, this parameter must be considered in addition, for the double-D winding. Furthermore, a parallel connection of the two coils of the double-D winding or the use of a dedicated converter for regulating the phase shift between the currents in the two coils constitutes another degree-of-freedom for this IPT coil geometry [32]. However, such a configuration is not considered in this paper in order to maintain the focus on the fundamental differences between the two IPT coil geometries. Hence, the two coils are always series connected with opposite orientation of the currents as shown in Fig. 2(d).

In order to limit the number of necessary FEM simulation steps, the dimensions of the ferrite rods  $d_{\text{fe}}$ ,  $h_{\text{fe}}$ , and the specifications of the litz wire are kept constantly at the values of the I-126/20 K2004 ferrite cores [33] and the  $2500 \times 0.1$  mm litz wire used in [17].

Using the design space in Table I, calculations for all the parameter combinations are executed. For each design point, the number of turns of the IPT coils is adjusted such that the self-inductances  $L_1$  and  $L_2$  of the transmitter

TABLE I  
DESIGN SPACE FOR THE MULTI-OBJECTIVE OPTIMIZATION

Variable	Min. (mm)	Max. (mm)	Step (mm)	#Points (-)
$W_{\text{coil}}$	300	700	50	9
$L_{\text{coil}}$	300	700	50	9
$d_{\text{cu}}$	50	150	25	5
$w_{\text{cu}}$	50	150	25	5
$w_{\text{cu,in}}$	50	150	25	5
$N_{\text{fe}}$	3	7	2	3

and the receiver coil, respectively, fulfill the design rules [18], [28], [29]

$$L_2 \approx \frac{R_{L,\text{eq}}}{\omega_0 k} \quad \text{and} \quad L_1 \approx L_2 \left( \frac{U_{1,\text{dc}}}{U_{2,\text{dc}}} \right)^2 \quad (2)$$

where  $i \in [1, 2]$  stands for the transmitter or the receiver coil, respectively,  $R_{L,\text{eq}} = 8/\pi^2 \cdot U_{2,\text{dc}}^2/P_2$  stands for the equivalent load resistance of the fundamental frequency model [34], and  $\omega_0$  is the resonant frequency. It is shown in [18], [28], and [29] that IPT coil designs that fulfill (2) achieve the maximum transmission efficiency given by (1) at the resonant frequency  $\omega_0$ , the dc input voltage  $U_{1,\text{dc}}$ , the dc output voltage  $U_{2,\text{dc}}$ , and the output power  $P_2$ .

The resonant capacitors  $C_1$  and  $C_2$  are designed for a full compensation of the coil self-inductances by  $C_i \approx 1/(\omega_0^2 L_i)$  with  $i \in [1, 2]$  at the transmission frequency of 85 kHz. The resonant capacitors are connected in series to the IPT coils on both sides of the air gap. The series-series compensation is preferred in this paper because of the higher efficiency during partial load conditions and because the fully symmetric topology simplifies the experiments with energy feedback presented in Section IV. The results of the IPT coil geometry comparison discussed in this section are expected to apply similarly also if one or both the compensation capacitors are connected in parallel to the respective IPT coil.

For the hardware prototypes of Section IV, polypropylene film capacitors of the series CSP 120-200 [31] are considered. The capacitance values are slightly increased in order to shift the zero phase angle frequency downward, such that the resonant circuit exhibits an inductive input impedance and zero voltage switching of the transmitter-side power semiconductors of the transmitter-side silicon-carbide (SiC) power MOSFET devices is achieved at the is achieved at the transmission frequency.

### C. Discussion of Optimization Results

The calculation results are shown in Fig. 5. The definitions for the transmission efficiency (or ac-ac efficiency) are  $\eta = P_2/(P_2 + P_{\text{loss}})$ , where  $P_2 = 50$  kW is the output power and  $P_{\text{loss}}$  stands for the total power losses in the resonant circuit. The area-related power density is given by  $\alpha = P_2/A_{\text{coil}}$  and the gravimetric power density is  $\gamma = P_2/m_{\text{coil}}$ , where  $A_{\text{coil}} = L_{\text{coil}}W_{\text{coil}}$  is the coil area and  $m_{\text{coil}}$  stands for the total mass of the active materials. It shall be emphasized that the efficiency  $\eta$  includes only the resonant

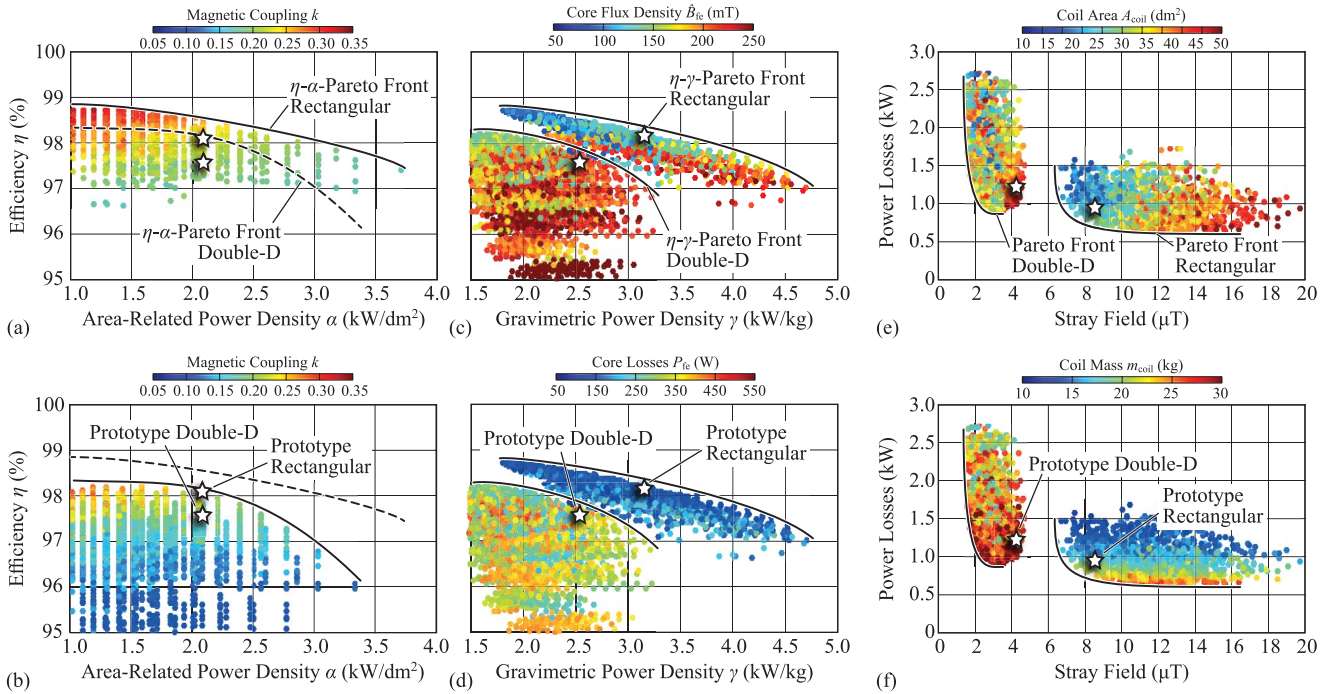


Fig. 5. Results of the 50 kW/85 kHz multi-objective IPT coil optimization with rectangular or double-D winding geometry. (a) and (b)  $\eta$ - $\alpha$ - and (c) and (d)  $\eta$ - $\gamma$ -Pareto plane. (e) and (f) FEM-calculated magnetic stray field at 1.1-m distance from the coil center. The parameters for the coloring are (a) and (b) magnetic coupling  $k$ , (c) core flux density  $\hat{B}_{fe}$ , (d) total core losses  $P_{fe}$ , (e) coil area  $A_{coil}$ , and (f) coil mass  $m_{coil}$ . Included are the coil area, the mass, and the power losses of the active coil materials (litz wire winding, ferrite cores, eddy current shielding), and the resonant capacitors.

components of the IPT system, i.e., the power losses in the windings, the cores, the shielding, and the resonant capacitors, while the losses of the power converter are not included.

From the  $\eta$ - $\alpha$ -Pareto plane shown in Fig. 5(a) and (b), it becomes apparent that the attainable magnetic coupling is higher for the rectangular winding than for the double-D winding. Therefore, the double-D coil geometry shows an approximately 0.5%-points lower transmission efficiency  $\eta$  for the same area-related power density  $\alpha$ , i.e., for the same outer coil dimensions. The two hardware prototypes are also indicated in the Pareto planes in Fig. 5. The prototypes are realized in the same coil housing. Therefore, they have the same area-related power density, but different gravimetric power density  $\gamma$  as a result of the modified winding.

The  $\eta$ - $\gamma$ -Pareto plane in Fig. 5(c) and (d) shows that for the IPT coil geometry with a double-D winding, the gravimetric power density  $\gamma$  is lower for the same transmission efficiency. If designs with the same gravimetric power density are compared, a design with double-D winding is approximately 1%-points less efficient than a design with rectangular winding. The reason for the mass difference is the larger copper and core volumes. For the double-D coil geometry, the core flux density  $\hat{B}_{fe}$  is typically higher and more core material is needed (see Fig. 5(c)). In fact, only designs with  $N_{fe} \in [5, 7]$  core rods are possible due to core saturation, while for the rectangular winding also designs with  $N_{fe} = 3$  are feasible. Therefore, the IPT coil geometry with the rectangular winding is realizable with a lighter core structure.

As a result of the higher flux density in the core, also the total core losses  $P_{fe}$  are increased for the double-D winding

(see Fig. 5(d)). The FEM simulation results obtained for the two prototypes shown in Fig. 6(a) and (b) confirm that the additional losses result from the high flux density in the central region of the ferrite cores. As shown in Fig. 6(c), the calculated power losses are approximately 50% higher for the prototype with double-D winding, due to the increased core losses. In Fig. 6(c),  $i \in [1, 2]$  stands for the transmitter or the receiver coil, respectively, and the variable  $P_{cu,i}$  stands for the litz wire winding losses  $P_{fe,i}$  for the core losses, and  $P_{sh,i}$  for the eddy current losses in the shielding. The total power losses inside the coil housing are given by the sum of the winding losses and the core losses. They add up to 247 and 422 W for the transmitter coil with rectangular winding and double-D winding, respectively. In the case of a coil misalignment, the total losses inside the coil housing are increased further. Because the housing is made exclusively from plastics with low thermal conductivity, some air flow is required to limit the heating of the litz wire and the ferrite cores. Therefore, either side of the coil housing is equipped with an array of cooling fans for forced convection cooling (see Fig. 1).

The key advantage of the double-D winding becomes apparent when comparing the magnetic stray field of the two coil geometries. Fig. 5(e) and (f) shows the total power losses in the resonant circuit as a function of the magnetic stray field at a fixed reference point at 1.1 m distance from the coil center (critical distance in the considered industry application) on a horizontal axis in the lateral direction, starting at the air gap center point (see Fig. 7 for axis orientations). As expected from the conceptual analysis of Section II-B, the stray field is significantly reduced for the double-D winding (C-type),

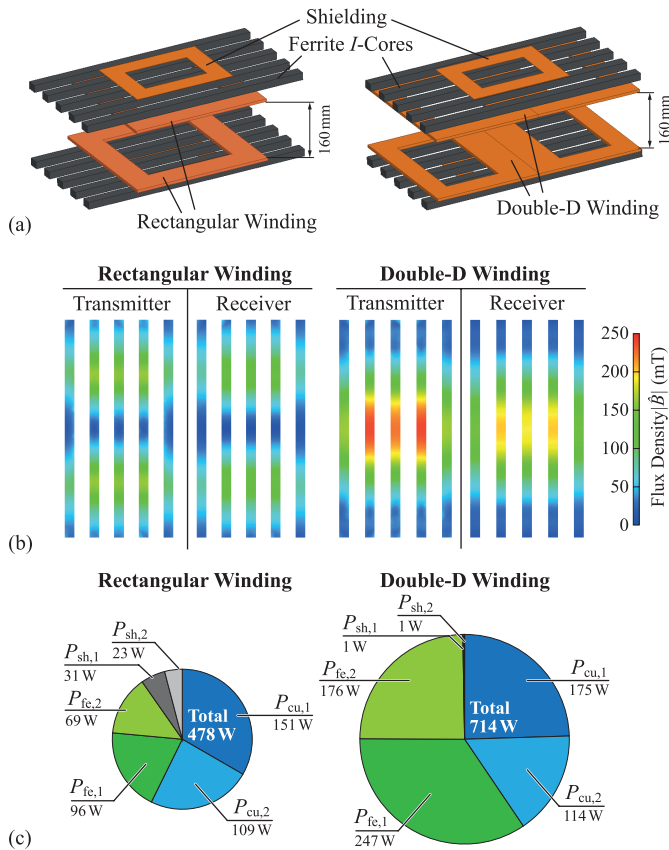


Fig. 6. (a) Simulation models and (b) FEM-calculated magnetic flux density in the cores of the prototype IPT coils with rectangular and double-D winding. (c) Calculated power losses of the prototypes at 50 kW output power (drawn to scale).

because the complete reluctance path is included within the coil structure. Since for the rectangular winding (E-type) the surrounding environment is part of the magnetic circuit, the field at the reference point is up to three times higher than for the double-D winding. However, the required coil area and coil mass is higher for the double-D winding, as shown by the coloring in Fig. 5(e) and (f).

Comparing the power loss distribution of the two hardware prototypes in Fig. 6(c) shows that for the double-D winding, the losses in the eddy current shielding are significantly reduced. Due to the opposite winding sense of the two coils that form the double-D and their magnetic connection with the low-reluctance ferrite cores, the flux is naturally guided along the core without much leakage. With the rectangular winding, the core does not significantly lower the reluctance seen by the field lines that spread out on the sides of the E-type coil geometry in Fig. 2(c). Therefore, the eddy current shielding is necessary to block the path for the flux at the backside of the coil and reduce the field leakage. The power losses in the shielding are acceptable in practice, because they do not require additional cooling as long as the employed material is sufficiently conductive [19]. For the hardware prototypes, the shielding is realized with a  $210 \times 280 \text{ mm}^2$  plate of 2 mm thickness manufactured from oxygen-free copper with a conductivity of approximately 43 MS/m at room temperature. A discussion of the alternative shielding methods can be found in [24].

TABLE II  
DESIGN PARAMETERS OF THE REALIZED IPT COIL PROTOTYPES

Variable	Rectangular	Double-D
$W_{\text{coil}}$ (mm)	380	380
$L_{\text{coil}}$ (mm)	630	630
$d_{\text{cu}}$ (mm)	125	18
$w_{\text{cu}}$ (mm)	67.5	56
$w_{\text{cu,in}}$ (mm)	n/a	90
$N_{\text{fe}}$	5	5
$N_1, N_2^{1,2}$	9.5	6.5
Litz wire	2500 x 0.1 mm	
Ferrite cores	I-126/20, K2004	
Resonant caps.	CSP 120-200	
Shielding	OFC, 2 mm thick	

<sup>1</sup>Turns number "x.5" means that connections are at opposite sides of winding. <sup>2</sup>Double-D turns number is given for one of the two coils of a winding.

The results presented in this section confirm what was expected from the conceptual analysis in Section II-B. They also show that a coil optimization that takes only the magnetic coupling into account is inaccurate. For instance, the core losses have a high impact on the performance, which is not captured when looking only at the magnetic coupling. Furthermore, the observed Pareto tradeoffs demonstrate that an analysis based on a single realization example is insufficient. A multi-objective analysis is mandatory and only a comparison of the Pareto fronts of the different IPT coil geometries can fully clarify their advantages and disadvantages.

#### IV. EXPERIMENTAL RESULTS

In this section, comprehensive experimental results obtained from the two prototype IPT coils in Fig. 1 are presented. The main design parameters of the two prototypes are summarized in Table II. The same  $410 \times 760 \times 60 \text{ mm}^3$  coil housing and the same core structure is used for both the prototypes, such that the only difference is the geometry of the winding. Therefore, the presented measurements clearly show the impact of the modified winding geometry on the performance of the overall EV charging system. It shall be noted that in this discussion, the transmitter and the receiver IPT coils are always of the same winding geometry. Mixed arrangements with the double-D prototype as transmitter coil and the prototype with rectangular winding as receiver coil are not discussed herein.

##### A. Inductance and Magnetic Coupling

In a first step, the magnetic design is experimentally verified. Table III shows the measured and the FEM-calculated transformer equivalent circuit parameters for the prototypes for an air gap of 160 mm and the selected capacitance values required for the series-series resonant compensation of the self-inductances. In addition, the calculated dc and ac winding resistances as well as the quality factors are indicated. For the calculation of the quality factor, the definition in [18], [35]

$$Q = \sqrt{\prod_{i \in [1,2]} \frac{\omega_0 W_{L_i}}{P_{\text{cu},i} + P_{\text{fe},i} + P_{\text{sh},i}}} \quad (3)$$

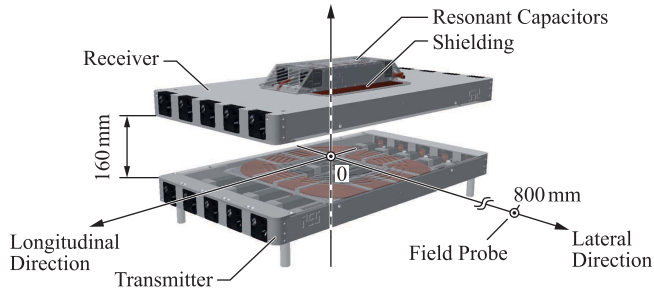


Fig. 7. IPT coil arrangement used for the experiments with indicated definitions of axis orientations used in the text. Details of the design of the resonant capacitor module and the shielding can be found in [19] and [21].

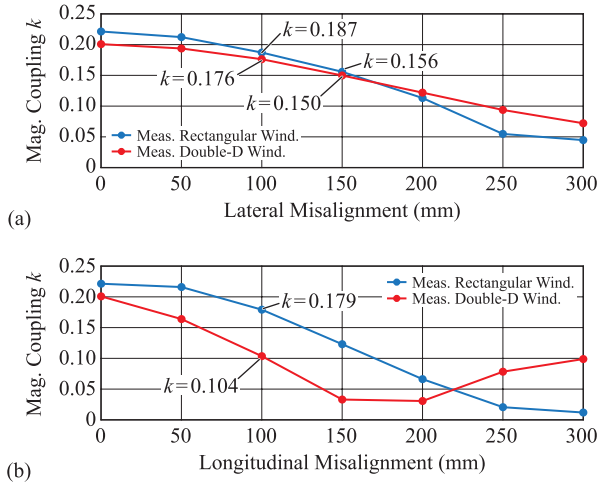


Fig. 8. Measurements of the magnetic coupling with (a) lateral and (b) longitudinal misalignment (see Fig. 7 for axis orientation) of the receiver coil at an air gap of 160 mm.

is employed, where  $i \in [1, 2]$  stands for the transmitter or the receiver coil, respectively, and  $W_{L_i}$  represents the peak stored magnetic energy in the inductor  $L_i$  at a 50 kW output power. In this way, also the losses in the core  $P_{fe,i}$  and the eddy current shielding  $P_{sh,i}$  are incorporated in addition to the winding losses  $P_{cu,i}$ . A good match between the calculated and measured values is observed, despite the simplified FEM models of Fig. 6(a). Furthermore, the similar inductance values ensure comparable impedance conditions in the resonant circuit and therefore similar ac transfer functions. This further improves the comparability of the presented experiments.

Measurements of the magnetic coupling as a function of the horizontal coil misalignment are shown in Fig. 8. The IPT coil arrangement used during the measurements and the definition of the axis orientations used below is shown in Fig. 7. The magnetic coupling is determined from the open-circuit and short-circuit inductance measurements obtained from an impedance analyzer. For ideally positioned IPT coils, the magnetic coupling is slightly lower for the double-D prototype. A lateral coil misalignment causes a comparable decrease in magnetic coupling for both the prototypes. For a coil misalignment in the longitudinal direction, the magnetic coupling drops much faster for the double-D prototype. This is a result of the smaller enclosed coil area of the two windings, which already

TABLE III  
MEASURED AND FEM-CALCULATED EQUIVALENT CIRCUIT  
PARAMETERS FOR THE IPT COIL PROTOTYPES

Variable	Rectangular		Double-D	
	Meas.	FEM	Meas.	FEM
$L_1$ ( $\mu\text{H}$ )	68.2	71.6	64.5	65.5
$L_2$ ( $\mu\text{H}$ )	70.6	71.6	64.5	65.5
$M$ ( $\mu\text{H}$ )	15.4	16.5	12.6	15.7
$k$	0.2214	0.2318	0.2008	0.2399
$C_1$ (nF)	54.1		54.1	
$C_2$ (nF)	54.1		54.1	
$R_{DC}$ (m $\Omega$ )	14.3		16.4	
$R_{AC}$ (m $\Omega$ )	22.5		23.7	
$R_{AC}/R_{DC}$	1.57		1.44	
$Q$	921		594	
$FOM$	212		143	

at a small longitudinal coil misalignment have much less overlap.

In [12], it is proposed to add a 90°-rotated winding around the core of the IPT receiver coil, termed as the *quadrature* winding. The auxiliary winding has an improved magnetic coupling to the transmitter in the misaligned position and can therefore improve the positioning tolerance. It is connected to the receiver-side dc-link via a separate rectifier unit. Hence, additional power electronic components are required and a dedicated control might be needed in practice in order to suppress the circulating reactive currents between the two receiver coils. This modification therefore increases the complexity and adversely affects the power density of this coil geometry. Therefore, this is not investigated further in this paper.

### B. DC–DC Efficiency

The experimental setup and the power electronic converter in [21] are used for the efficiency measurements. The details of the converter design can be found in [19] and [21], therefore only a brief overview is given herein.

The converter shown in Fig. 9(a) comprises an interleaved buck+boost-type dc–dc conversion stage with coupled magnetic devices, which produces a variable dc-link voltage ( $U_{1,dc}$  or  $U_{2,dc}$ ) of up to 800 V from a fixed dc input voltage of 600 V. This conversion stage is realized with SiC MOSFET devices of type C2M0080120D (1.2 kV/80 m $\Omega$ ), which are hard-switched at 50 kHz. A full-bridge inverter is used to generate a fixed-frequency rectangular voltage waveform, which is directly applied to the series-series compensated IPT resonant circuit. In this conversion stage, three SiC MOSFET devices of type C2M0025120D (1.2 kV/25 m $\Omega$ ) are used in parallel connection with a single gate driver for each switch of the full-bridge inverter. The converter is manufactured in duplicate and is used at the transmitter and at the receiver as shown in Fig. 9(b). On the receiver side, the full-bridge inverter stage is used as a synchronous rectifier to minimize the conduction losses of the power semiconductors. By simultaneously adjusting the dc-link voltages  $U_{1,dc}$  and  $U_{2,dc}$  at a fixed inverter

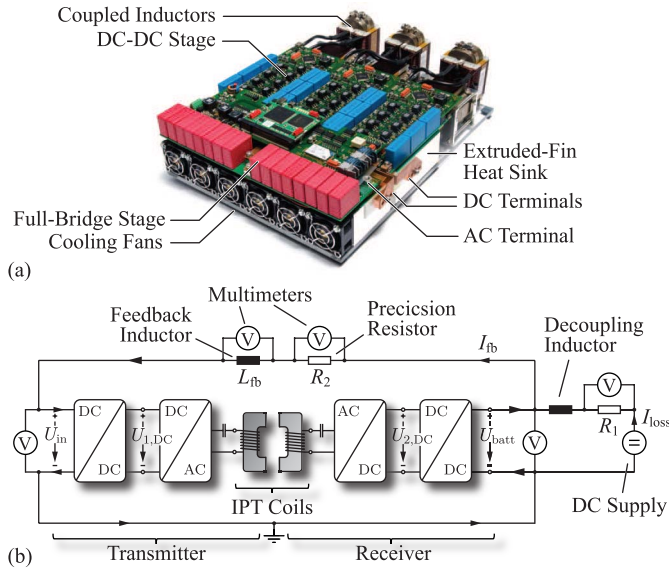


Fig. 9. (a) All-SiC power electronic converter used at the transmitter and receiver sides for control of the dc-link voltages  $U_{1,dc}$  and  $U_{2,dc}$  from a fixed supply voltage  $U_{batt} = 600$  V for regulating the power flow in the IPT system. (b) Experimental setup with energy feedback for direct power loss measurements at up to 50 kW output power (reproduced from [21]).

switching frequency, the power flow to the output of the IPT system can be regulated with a high partial-load efficiency [18], [19], [36].

At the receiver-side dc output, a dc-supply is connected instead of an EV battery, via a decoupling inductor and a precision shunt resistor  $R_1 = 10$  m $\Omega$ . An energy feedback path is provided by the feedback inductor  $L_{fb} = 3.4$  mH and the precision shunt resistor  $R_2 = 1$  m $\Omega$ . In this setup, the transferred energy can be circulated in the system and no 50 kW ohmic load is required. The employed principle is similar to the back-to-back testing of a power transformer [37] or of two mechanically coupled electrical machines [38], which are supplied by two inverters with electrically connected dc-links (Hopkinson's or regenerative test). A direct power loss measurement is obtained by measuring the current  $I_{loss}$ , using the shunt resistor  $R_1$  and the voltage  $U_{batt}$ . Furthermore, the feedback current  $I_{fb}$  is measured using  $R_2$  in order to determine the output power of the IPT system. In addition, the voltage drop on the feedback inductor  $L_{fb}$  is measured and the dc losses of the inductor are subtracted from the power loss measurement. In this way, the dc–dc efficiency, including all power conversion stages between  $U_{in}$  and  $U_{batt}$ , can be determined with a high accuracy.

The measurement results for the dc–dc efficiency of the prototypes at an air gap of 160 mm are shown in Fig. 10 as a function of the output power. The dc–dc efficiency of both the IPT coil geometries is similar for ideally positioned IPT coils and at lateral coil misalignment. For the nominal coil position, a dc–dc efficiency of approximately 95.8% is reached at a 50 kW power transfer ( $k \approx 0.22$ ). The flat efficiency curve is a result of the employed power control with variable dc-link voltages [19]. As expected, the dc–dc efficiency drops to 94% at 150 mm lateral coil misalignment ( $k \approx 0.15$ ).

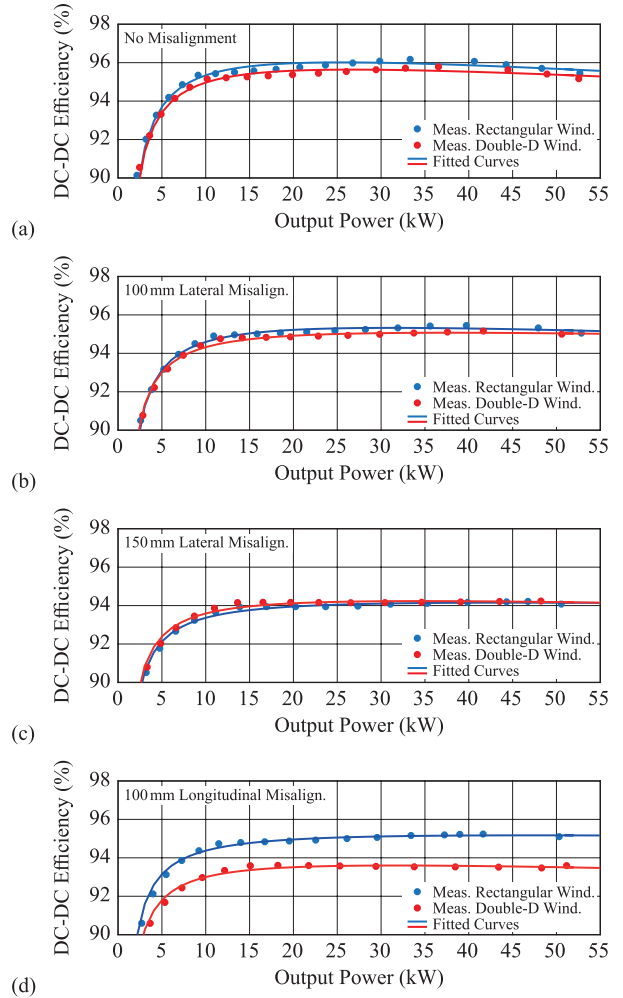


Fig. 10. Measured dc–dc efficiency at a 160 mm air gap and  $U_{batt} = 600$  V for (a) ideal coil positioning, (b) 100 mm, (c) 150 mm lateral coil misalignment, and (d) 100 mm longitudinal coil misalignment (see Fig. 7 for axis orientation).

The impact of the IPT coil geometry on the dc–dc efficiency is only a concern at a longitudinal coil misalignment. As expected from Fig. 8(b), the efficiency of the double-D prototype is lower, due to the significantly reduced magnetic coupling  $k \approx 0.1$  at a longitudinal coil misalignment of 100 mm. Without auxiliary quadrature winding and the necessary additional power electronics and control equipment used in [12], the positioning tolerance of the double-D prototype is inferior to that of the prototype with rectangular winding.

### C. Magnetic Stray Field

According to the presented FEM calculations, a lower magnetic stray field is the main advantage of the IPT coil geometry with double-D winding. Therefore, measurements of the magnetic flux density are conducted at a reference point at an 800 mm lateral distance measured from the transmitter coil center (distance where rectangular winding prototype fulfills ICNIRP2010). The measurements are taken with the field probe designed in [39], which is shown in Fig. 11(b). The experiment is repeated for a lateral misalignment of the receiver coil 150 mm away from the field probe.

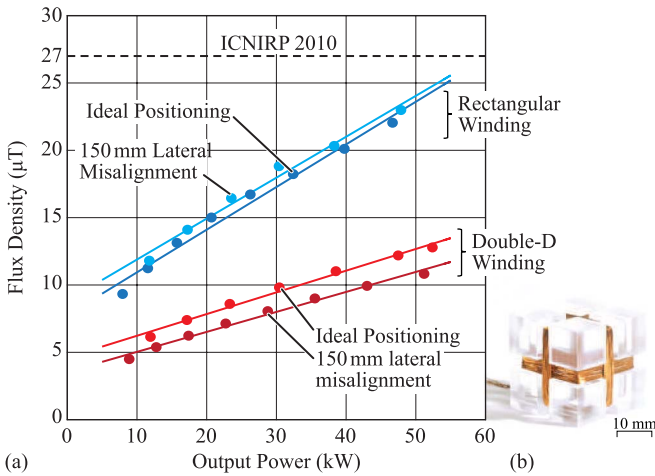


Fig. 11. (a) Magnetic stray field (rms value) at 800 mm lateral distance from the air gap center point, with ideally positioned IPT coils and with 150 mm lateral misalignment of the receiver coil away from the field probe (see Fig. 7 for axis orientation). (b) Field probe designed in [39], which is used for the shown measurements.

The results are shown in Fig. 11(a) together with the reference level for the general public given in the ICNIRP 2010 standard [5]. The measurements confirm that for the double-D prototype, the stray field is reduced by approximately a factor of two across the whole power range. This is clearly a significant advantage of the IPT coil geometry with double-D winding.

## V. CONCLUSION

In this paper, the IPT coil prototype with rectangular winding designed in [17] is compared with an IPT coil geometry with double-D winding and the same outer dimensions. The main advantages and disadvantages of the two IPT coil geometries are discussed with the help of Pareto analysis, and with a comprehensive experimental investigation of the two hardware prototypes.

On the one hand, a double-D winding results in an approximately 0.5%-points lower transmission efficiency for the same area-related power density, i.e., for the same footprint area of the IPT coil on the vehicle. Furthermore, at the same gravimetric power density, designs with a double-D winding are approximately 1%-points less efficient than designs with rectangular winding. Both effects are caused by additional core losses that result from the increased core flux density of the IPT coil geometry with double-D winding. On the other hand, the magnetic stray field observed at a fixed reference point is up to a factor of two higher for a rectangular winding. Experiments confirm this clear advantage of the double-D IPT coil geometry.

Measurements of the dc–dc efficiency, including the power electronics, show that the performance of the two hardware prototypes is comparable at an ideal coil positioning and for lateral coil misalignment. At a longitudinal coil misalignment, the performance of the double-D prototype is inferior due to the faster decaying magnetic coupling. Methods exist in the literature for counteracting this effect, however, they require auxiliary components that decrease the power density and increase the complexity of the IPT system.

All in all, a tradeoff results for high-power EV charging. For a practical system, it must be analyzed if the power losses, the positioning tolerance, or the stray field are the limiting factors. At a high power level, where the thermal management makes high efficiency crucial, or for applications that require lightweight on-board power electronics equipment, a geometry with a rectangular winding is appropriate. However, if the safety standards for the magnetic stray field should be met at a short distance from the coil, an IPT coil geometry with double-D winding should be selected.

## ACKNOWLEDGMENT

The authors would like to thank ABB Switzerland Ltd. for their support regarding many aspects of this research project.

## REFERENCES

- [1] B. Warner, O. Augé, and A. Moghstaei, "Taking charge—Flash charging is just the ticket for clean transportation," *ABB Rev.*, no. 4, pp. 64–69, 2013, accessed on Feb. 24, 2016. [Online]. Available: <http://www.abb.com/>
- [2] Siemens AG. (2015). *Charging Your Future—With the Siemens eBus Charging Infrastructure*, accessed on Sep. 16, 2015. [Online]. Available: [www.siemens.com/mobility](http://www.siemens.com/mobility)
- [3] Wave IPT. (2015). *Wirelessly Charging Electric Vehicles*, accessed on Sep. 16, 2015. [Online]. Available: [www.waveipt.com](http://www.waveipt.com)
- [4] Bombardier Transportation. (2013). *Primove—Introducing True Electric Mobility for a Sustainable Future*, accessed on Sep. 16, 2015. [Online]. Available: <http://primove.bombardier.com>
- [5] International Commission on Non-Ionizing Radiation Protection (ICNIRP), "Guidelines for limiting exposure to time-varying electric and magnetic fields (1 Hz to 100 kHz)," *Health Phys.*, vol. 99, no. 6, pp. 818–836, 2010.
- [6] Y. Nagatsuka, N. Ehara, Y. Kaneko, S. Abe, and T. Yasuda, "Compact contactless power transfer system for electric vehicles," in *Proc. Int. Power Electron. Conf. (IPEC)*, Sapporo, Japan, Jun. 2010, pp. 807–813.
- [7] L. K. L. Cheng, J. W. Hay, and P. G. W. Beart, "Contact-less power transfer," U.S. Patent 6906495 B2, Jun. 14, 2005.
- [8] J. T. Boys, G. A. Covic, and M. B. Budhia, "Inductive power transfer apparatus," WO Patent 2012018268 A1, Feb. 9, 2012.
- [9] M. Budhia, G. A. Covic, and J. T. Boys, "A new IPT magnetic coupler for electric vehicle charging systems," in *Proc. 36th Annu. Conf. IEEE Ind. Electron. Soc. (IECON)*, Glendale, AZ, USA, Nov. 2010, pp. 2487–2492.
- [10] M. Budhia, G. A. Covic, and J. T. Boys, "Design and optimization of circular magnetic structures for lumped inductive power transfer systems," *IEEE Trans. Power Electron.*, vol. 26, no. 11, pp. 3096–3108, Nov. 2011.
- [11] C.-Y. Huang, "Design of IPT EV battery charging systems for variable coupling applications," Ph.D. dissertation, Dept. Elect. Comput. Eng., Univ. Auckland, Auckland, NZ, USA, 2011.
- [12] M. Budhia, J. T. Boys, G. A. Covic, and C.-Y. Huang, "Development of a single-sided flux magnetic coupler for electric vehicle IPT charging systems," *IEEE Trans. Ind. Electron.*, vol. 60, no. 1, pp. 318–328, Jan. 2013.
- [13] G. Ombach, D. Kürschner, S. Mathar, and W. Chlebosz, "Optimum magnetic solution for interoperable system for stationary wireless EV charging," in *Proc. 10th Int. Conf. Ecol. Veh. Renew. Energies (EVER)*, Monte Carlo, Monaco, Mar./Apr. 2015, pp. 1–8.
- [14] D. Kürschner, F. Turki, C. Yotta, S. Thamm, and C. Rathge, "Comparison of planar and solenoid coil arrangements for inductive EV-charging application," in *Proc. Conf. Power Convers. Intell. Motion (PCIM Europe)*, Nuremberg, Germany, May 2013, pp. 385–391.
- [15] L. Ming and K. D. T. Ngo, "Comparison of coil designs for wireless inductive power transfer," in *Proc. Center Power Electron. Syst. Conf. (CPES)*, Blacksburg, VA, USA, Apr. 2014.
- [16] K. Knaisch and P. Gratzfeld, "Comparison of magnetic couplers for inductive electric vehicle charging using accurate numerical simulation and statistical methods," in *Proc. 5th Int. Electr. Drives Prod. Conf. (EDPC)*, Nuremberg, Germany, Sep. 2015, pp. 1–10.

- [17] R. Bosshard and J. W. Kolar, "Multi-objective optimization of 50 kW/85 kHz IPT system for public transport," *IEEE J. Emerg. Sel. Topics Power Electron.*, 2016.
- [18] R. Bosshard, J. W. Kolar, J. Mühlethaler, I. Stevanović, B. Wunsch, and F. Canales, "Modeling and  $\eta$ - $\alpha$ -Pareto optimization of inductive power transfer coils for electric vehicles," *IEEE J. Emerg. Sel. Topics Power Electron.*, vol. 3, no. 1, pp. 50–64, Mar. 2015.
- [19] R. Bosshard, "Multi-objective optimization of inductive power transfer systems for EV charging," Ph.D. dissertation, Dept. Inf. Technol. Elect. Eng., ETH Zürich, Zürich, Switzerland, 2015.
- [20] *Wireless Charging of Electric and Plug-in Hybrid Vehicles*, SAE Standard J2954, Society of Automotive Engineers, accessed on Sep. 16, 2015. [Online]. Available: <http://standards.sae.org/wip/j2954/>
- [21] R. Bosshard and J. W. Kolar, "All-SiC 9.5 kW/dm<sup>3</sup> on-board power electronics for 50 kW/85 kHz automotive IPT system," 2016.
- [22] B. Goeldi, J. Tritschler, and S. Reichert, "Measurement results of a 22 kW bidirectional inductive charger," in *Proc. Int. Exhibit. Conf. Power Electron., Intell. Motion, Renew. Energy Energy Manage. (PCIM Europe)*, Nuremberg, Germany, May 2015, pp. 1–8.
- [23] T. Diekhans and R. W. D. Doncker, "A dual-side controlled inductive power transfer system optimized for large coupling factor variations and partial load," *IEEE Trans. Power Electron.*, vol. 30, no. 11, pp. 6320–6328, Nov. 2015.
- [24] J. Kim *et al.*, "Coil design and shielding methods for a magnetic resonant wireless power transfer system," *Proc. IEEE*, vol. 101, no. 6, pp. 1332–1342, Jun. 2013.
- [25] J. Huh, S. W. Lee, W. Y. Lee, G. H. Cho, and C. T. Rim, "Narrow-width inductive power transfer system for online electrical vehicles," *IEEE Trans. Power Electron.*, vol. 26, no. 12, pp. 3666–3679, Dec. 2011.
- [26] F. Turki, R. Wiengarten, V. Reising, and A. Kratser, "Impact of the working frequency on wireless power transfer systems," in *Proc. Int. Exhibit. Conf. Power Electron., Intell. Motion, Renew. Energy Energy Manage. (PCIM Europe)*, Nuremberg, Germany, May 2014, pp. 1–6.
- [27] J. C. Schuder, "Powering an artificial heart: Birth of the inductively coupled-radio frequency system in 1960," *Artif. Organs*, vol. 26, no. 11, pp. 909–915, Jun. 2002.
- [28] K. van Schuylenbergh and R. Puers, *Inductive Powering: Basic Theory and Application to Biomedical Systems*, 1st ed. Dordrecht, The Netherlands: Springer, 2009.
- [29] E. Waffenschmidt and T. Staring, "Limitation of inductive power transfer for consumer applications," in *Proc. 13th Eur. Conf. Power Electron. Appl. (EPE)*, Barcelona, Spain, Sep. 2009, pp. 1–10.
- [30] J. Mühlethaler, "Modeling and multi-objective optimization of inductive power components," Ph.D. dissertation, Dept. Inf. Technol. Elect. Eng., ETH Zürich, Zürich, Switzerland, 2012.
- [31] Celelem Power Capacitors Ltd. (2015). *CSP 120/200 Data Sheet*, accessed on Jun. 17, 2016. [Online]. Available: [www.celelem.com](http://www.celelem.com)
- [32] G. A. Covic, M. L. G. Kissin, D. Kacprzak, N. Clausen, and H. Hao, "A bipolar primary pad topology for EV stationary charging and highway power by inductive coupling," in *Proc. IEEE Energy Convers. Congr. Expo. (ECCE)*, Phoenix, AZ, USA, Sep. 2011, pp. 1832–1838.
- [33] Kaschke Components GmbH. (2015). *I-Kern I 126/20 Data Sheet*, accessed on Jun. 17, 2016. [Online]. Available: [www.kaschke.de](http://www.kaschke.de)
- [34] R. L. Steigerwald, "A comparison of half-bridge resonant converter topologies," *IEEE Trans. Power Electron.*, vol. 3, no. 2, pp. 174–182, Apr. 1988.
- [35] R. W. Erickson and D. Maksimovic, *Fundamentals of Power Electronics*, 2nd ed. New York, NY, USA: Springer, 2001.
- [36] B. Goeldi, S. Reichert, and J. Tritschler, "Design and dimensioning of a highly efficient 22 kW bidirectional inductive charger for E-mobility," in *Proc. Int. Exhibit. Conf. Power Electron., Intell. Motion, Renew. Energy Energy Manage. (PCIM Europe)*, Nuremberg, Germany, 2013, pp. 1496–1503.
- [37] G. Ortiz, "High-power DC-DC converter technologies for smart grid and traction applications," Ph.D. dissertation, Dept. Inf. Technol. Elect. Eng., ETH Zürich, Zürich, Switzerland, 2014.
- [38] B. Wrzeczionko, D. Bortis, and J. W. Kolar, "A 120 °C ambient temperature forced air-cooled normally-off SiC JFET automotive inverter system," *IEEE Trans. Power Electron.*, vol. 29, no. 5, pp. 2345–2358, May 2014.
- [39] R. Bosshard, J. W. Kolar, and B. Wunsch, "Accurate finite-element modeling and experimental verification of inductive power transfer coil design," in *Proc. 29th Appl. Power Electron. Conf. Expo. (APEC)*, Fort Worth, TX, USA, 2014, pp. 1648–1653.



**Roman Bosshard** (S'10) received the M.Sc. and Ph.D. degrees from the Swiss Federal Institute of Technology (ETH) Zürich, Zürich, Switzerland, in 2011 and 2015, respectively.

He joined the Power Electronic Systems Laboratory, ETH Zürich, in 2011, where he was a Ph.D. Student and later a Post-Doctoral Researcher. In 2016, he joined ABB Switzerland Ltd., Zürich, as a Power Electronics Development Engineer. During his studies, he focused on power electronics, ultrahigh-speed electrical drives, and control of mechatronic systems. His current research interests include inductive power transfer systems, high-power converter systems, SiC wide bandgap power devices, and electric drive systems.



**Ugaitz Iruretagoyena** received the B.Sc. degree in industrial electronics and the M.Sc. degree in energy and power electronics from the University of Mondragón, Mondragón, Spain, in 2012 and 2014, respectively, and the Ph.D. degree in collaboration with the Department of Systems Engineering & Control, University of the Basque Country, (UPV-EHU), Donostia, Spain.

He has been a Researcher with the IKERLAN-IK4 Technological Research Center, Mondragón, since 2014. His current research interests include the application of power electronic devices to the distribution network and electrical traction, as well as magnetic elements and induction power transfer.



**Johann W. Kolar** (M'89–SM'04–F'10) is currently a Full Professor and the Head of the Power Electronic Systems Laboratory with the Swiss Federal Institute of Technology (ETH) Zürich, Zürich, Switzerland. He has authored over 650 scientific papers in international journals and conference proceedings and holds more than 120 patents. His current research interests include ultracompact and ultraefficient SiC and GaN converter systems, wireless power transfer, solid-state transformers, power supplies on chip, and ultrahigh speed and bearingless

motors.

Johann Kolar received 21 IEEE TRANSACTIONS and Conference Prize Paper Awards and the ETH Zürich Golden Owl Award for excellence in teaching.